Chapter 12

REMOTE SENSING OF THE HIGH-LATITUDE IONOSPHERE
WITH COHERENT SCATTER HF RADAR:
A REVIEW OF THE TECHNIQUE AND RECENT WORK

J. M. Ruohoniemi, R. A. Greenwald, and K. B. Baker

The Johns Hopkins University Applied Physics Laboratory
Laurel, Maryland 20707

ABSTRACT

The high-latitude ionosphere is being studied with a new type of HF
radar. Facilities are now in operation at Goose Bay, Labrador, Schefferville,
Quebec, and Halley Station, Antarctica. In this paper, we review the HF
coherent scatter technique for the remote sensing of ionospheric structure and
dynamics. We describe the operation of the Goose Bay radar and the real-time
control of operating parameters that can be exercised during campaign periods.
We illustrate the methods for mapping ionospheric plasma convection. We
discuss recent findings on the generation of small-scale (~ 10 m)
irregularities in the E region by field-aligned currents and the occurrence of
irregularities in the wintertime F region trough at dusk. The dependence of
plasma convection in the dayside ionosphere on the IMF and the conjugate
relationship is illustrated with a case study involving the Goose Bay and
Halley Station radars. We also review recent work showing that the passage of
gravity waves in the neutral atmosphere is detected, extending the scope of
the HF radar studies to important questions of ionosphere-thermosphere
coupling.

INTRODUCTION

The high-latitude regions present unique opportunities for the study of
a wide range of problems in basic plasma physics and the interaction of the
solar wind with the earth's magnetosphere. It is known, for example, that
plasma instabilities are triggered by plasma drifts and density structures
that arise within the high-latitude regions (for a review, see Keskinen and
Ossakow [1983]). Also, large-scale electric fields generated within the outer
magnetosphere map to the ionosphere, primarily in the high-latitude zone. Of
particular interest to WITS, the interaction of the active ionosphere of the
auroral regions with the thermosphere is believed to be a major source of
energy for the neutral atmosphere.

In this paper, we describe a technique developed in this decade for the
study of high-latitude electrodynamics. It is based on the refraction and
scattering of high frequency (HF) radio signals within the ionosphere. The
experimental facilities, of which the Johns Hopkins University/Applied Physics
Laboratory (JHU/APL) radar located at Goose Bay, Labrador is the best-known
example, utilize electronic beam forming and steering for an exceptional
combination of spatial coverage (~ 10^6 km), spatial resolution (~ 50x50 km),
and temporal resolution (~ 1½ min). The HF radars at Schefferville, Quebec
and Halley Station, Antarctica have more recently become operational. The
Schefferville radar has a field of view that largely overlaps that of the
Goose Bay radar and the field of view of the Halley Station radar is
magnetically conjugate to that of Goose Bay. The use of the radars for
studying conjugate phenomena is referred to as the Polar Anglo-American
Conjugate Experiment (PACE). We illustrate with examples the range of studies
that can be carried out. In particular, the drift of ionospheric plasma
induced by electric fields is readily observed and can often be extensively

mapped. With this information, the drift conditions for the occurrence of irregularities can be analyzed. We present the results of recent work showing the relation of particular types of irregularity activity to ionospheric plasma drift. Of course, the mapping of high-latitude plasma convection is itself an important research goal. We show examples of convection maps and discuss the dependence of convection in the dayside ionosphere on the IMF. We conclude with a review of recent work on the effects of gravity waves on HF propagation and show that the Goose Bay radar in fact observes strong gravity wave disturbances.

HF Radio Wave Propagation

In the past, most coherent scatter studies of the ionosphere were performed with very high frequency (VHF) 30-300 MHz and ultrahigh frequency (UHF) 300-3000 MHz radars, which are essentially unaffected by changes in ionospheric properties. However, it has long been known that coherent scatter can also be obtained with high frequency (HF) 3-30 MHz radars [Bates and Albee, 1970]. At these lower frequencies the ionosphere has marked effects on the propagation of radar signals.

Figure 1 illustrates the manner in which VHF and HF radar signals are scattered by small-scale irregularity structures in the high-latitude E and F regions. The irregularities responsible for coherent scatter are aligned with the lines of force of the earth's magnetic field (see *Fejer and Kelley* [1980]). Signals from a VHF radar propagate in straight lines. If they encounter irregularities along their path, some of the energy in the incident wave will be scattered. If the scattered signals are to return to the radar, the incident wave must be directed normal to the irregularities in the region of interest and hence normal to the magnetic field. At very high latitudes, the direction of propagation of the probing radar signal must become nearly horizontal. This condition can be satisfied by a VHF radar in the E region but not in the F region. At HF frequencies the radar signal is refracted by the ionosphere toward the horizontal and the orthogonality condition can be satisfied in both the E and F regions.

It is necessary but not sufficient that the radar signal propagate orthogonal to B. Density structure of a scale that matches the radar sampling wavelength must also be present. The intensity of the backscattered signal is greatly increased if reflections from successive phase fronts of a density perturbation constructively interfere. This will occur if the scale length of the irregularity is half that of the radar wavelength. Thus, HF radars operating in the 8-20 MHz range of frequencies are sensitive to irregularities of scale length 7.5-19 m.

Coherent scatter radars are similar to incoherent scatter radars in that they sense density perturbations in the plasma density distribution. However, the perturbations responsible for incoherent scatter are generated by thermal fluctuations within the plasma, while the irregularities responsible for coherent scatter are amplified well above thermal levels by the action of plasma instabilities. Coherent scatter consequently does not require the high radar power levels associated with incoherent scatter, but the ability to make measurements depends more on the presence of irregularities within the plasma medium.

It will be clear from the preceding discussion that the successful operation of a coherent scatter HF radar requires an appropriate choice of transmitting frequency. This will need to be varied throughout the day as ionospheric conditions change, and also in accordance with solar cycle variations and storm-related ionospheric disturbances. Also, because complex modes of propagation are possible, it should be possible to vary the range interval for sampling returns. Thus the operating parameters of a coherent scatter HF radar must be kept flexible.
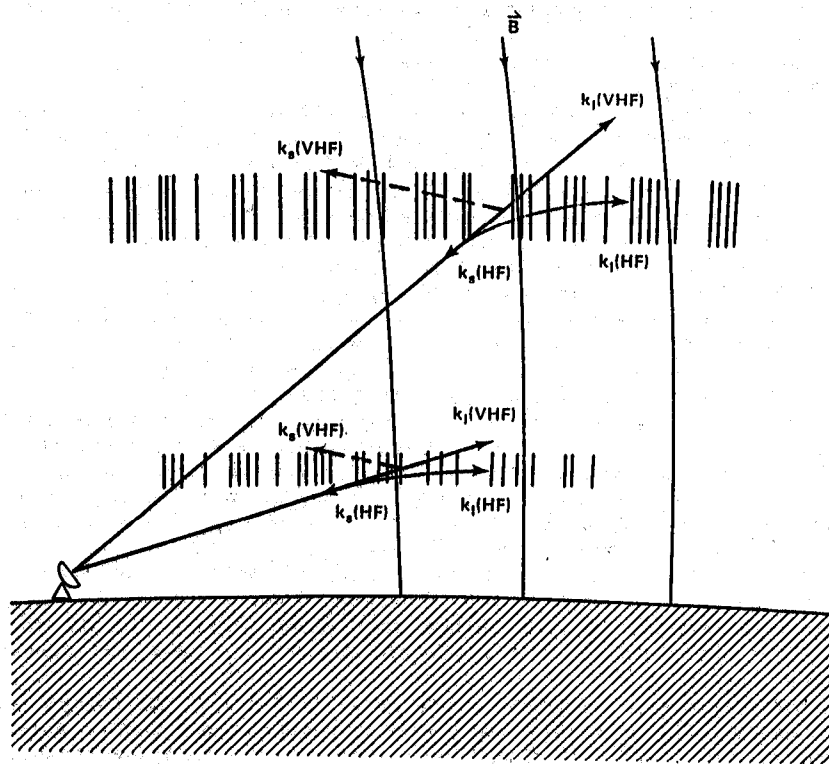
Figure 1. Illustration of the scattering of radar signals by ionospheric irregularities in the E and F regions. At VHF and higher frequencies the signals propagate in straight lines, while at HF frequencies they are refracted toward the horizontal. If the signals are propagating orthogonal to the magnetic field lines when they encounter a region of irregularities, some of the signal will be backscattered to the radar. [Reprinted from Greenwald et al., 1985]

In the next section, we briefly discuss the Goose Bay HF radar. The sister facilities at Schefferville, Quebec (Centre National de la Recherche Scientifique, France) and Halley Station, Antarctica (British Antarctic Survey) are basically similar. For a more detailed dicussion of the HF radar operations, see Greenwald et al. [1985].

HF Coherent Scatter Radar

The JHU/APL HF radar at Goose Bay, Labrador (53.4°N, 60.4°W) looks over northeastern Canada and Greenland (Figure 2). The radar consists of a pair of 16-element electronically steered arrays, where each element is a broadband (8-20 MHz) log periodic antenna. The arrays are 240 m long, 15 m above the ground, and separated by 100 m along the direction of the common array normal, which is directed 5° to the east of north. The narrow (~ 4°) antenna beam is scanned in a clockwise direction over a 50° azimuth sector through 16 evenly spaced pointing azimuths. The usual integration time for each beam position is 5-6 s and thus a single scan requires only 80-96 s. When the radar acts as vertical interferometer to measure the elevation angle of arrival by receiving on the two arrays simultaneously, the integration time is doubled. For each pointing azimuth, the returns from 50 range gates are sampled simultaneously. The gate separation is usually 30 or 45 km. The range to the first gate can be set to any value, but is generally close to 300 or 600 km.

The electronic steering of the antenna is accomplished with the broadband phasing matrix shown schematically in Figure 3. The principal elements of the phasing matrix are the eight branching networks known as 'phasing trees'. On transmission, signals enter a tree from the receiver side and pass through a network of power dividers and selected lengths of coaxial cable that ultimately produces successive time delays among the signals at the outputs. On receive, signals enter the tree from the antenna side and are reformed into a composite signal. Those signals arriving from the direction into which the antenna is directed will undergo constructive interference and exit the array at a considerably enhanced power level. The delay lines produce constant time delays rather than phase delays through the phasing matrix, and therefore the direction of the antenna beam is independent of frequency.

Each phasing tree produces one possible set of time delays across the antenna array. The 4-way switches shown in Figure 3 are used to select one of the phasing trees, and the double-pole double-throw (crossover) switches are used to determine whether the selected beam is directed to the right or left of the array normal. The properly phased signals are then directed to the T/R switch and chain of amplifier modules at the base of each antenna. The pulsed power level from each amplifier chain varies between 500 W and 1000 W, depending on frequency. (A modification to the transmitters will soon render the power level independent of frequency.) While the average peak radiated power from the array is thus only 10 kW, the array factors and antenna gain result in an effective radiated power of nearly 1 MW.

The radar transmits the seven-pulse pattern shown in Figure 4. An on-site microcomputer samples the backscattered signals from this pattern and calculates, in real-time, 17-lag complex autocorrelation functions (0 to 16 t_0). A seven-pulse pattern is sufficient to yield all the lags for the autocorrelation analysis. The autocorrelation data for the twenty range gates that return the strongest signal are stored on magnetic tape for further processing at APL.

The microcomputer at the station controls the radar as well as performs the preliminary processing of the incoming data. Two modes of operation are possible. In one, an operator who may be on-site or at a distant location equipped with a modem, enters operating parameters into the microcomputer. This mode is used for highly interactive real-time operation of the radar,
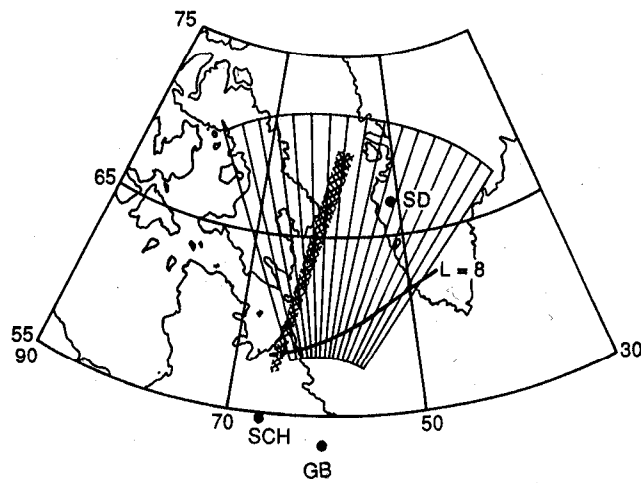
Figure 2. Field of view of the JHU/APL HF radar at Goose Bay (GB), Labrador. Also shown are the sites of the HF radar at Schefferville (SCH), Quebec, and the SRI incoherent scatter radar at Sondre Stromfjord (SD), Greenland. The field of view of the Goose Bay radar is divided into 16 sampling directions. The shaded area represents the sampling of the Schefferville radar on a single intersecting beam direction. [*Reprinted from Ruohoniemi et al., 1989*]

324

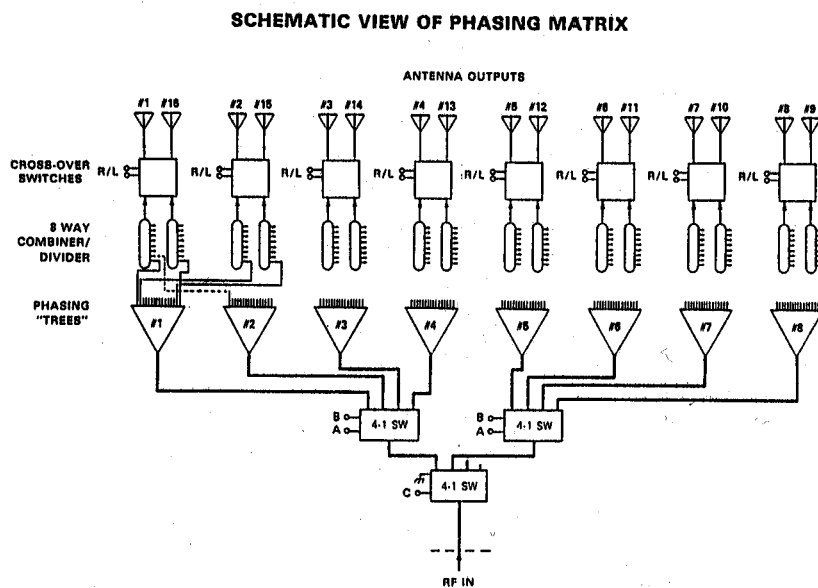**SCHEMATIC VIEW OF PHASING MATRIX**

Figure 3. Schematic diagram of the phasing matrix of the JHU/APL HF radar. A progressive time delay is established across the antenna array on transmission and reforms the beam on reception. [Reprinted from Greenwald et al., 1985]

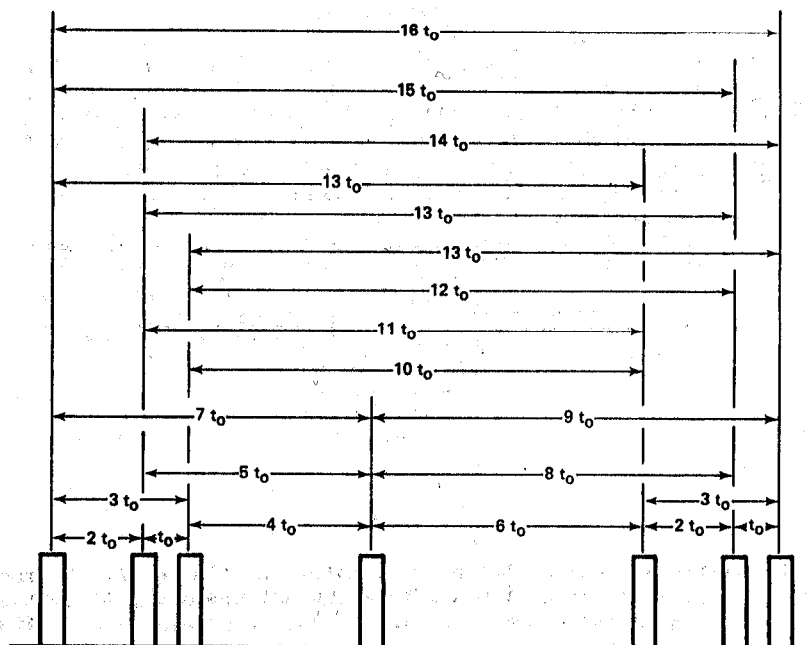# 7-PULSE PATTERN FOR 17-LAG AUTOCORRELATION FUNCTION

Figure 4. Seven-pulse transmission sequence used to determine 17-lag complex autocorrelation functions of the backscattered HF signals. Typically, $t_0 = 3.9$ ms. [Reprinted from Greenwald et al., 1985]

such as would be desirable during campaign periods. The other mode is used for noninteractive operation and consists of command strings that are stored on the disk in the form of text files. The strings determine the operating times, modes, and frequencies of the radar. They may be tailored to a particular type of study and supplied weeks or months in advance.

The Goose Bay radar began operation in 1983 and has run continuously (24-hr, 365 days/yr) since 1985 with occassional interruptions for system upgrades. The facility at Schefferville (54.8°N, 66.8°W) has operated in a limited way since 1987. The Halley Station radar (76°S, 27°W) has essentially operated like the Goose Bay radar (except for the vertical interferometer capability) since January, 1988.

We now turn to consideration of the information that can be gleaned from the HF coherent scatter returns. For more detailed discussions, see *Villain et al.* [1987] and *Baker et al.* [1988].

Signal Processing

The on-line analysis yields autocorrelation functions (ACFs) with real (R) and imaginary (I) parts. Ideally, these are damped cosine and sine functions, respectively. It is possible to Fourier transform the ACFs into 32-point Doppler spectra. However, it is advantageous to estimate the mean Doppler velocity and spectral width through direct analysis of the ACF. This is done by performing a linear least-squares fit of the phase angle [arctan(I/R)] as a function of the lag number. Figure 5 presents an example of an ACF (5a) and its phase angle variation (5c). It can be seen that there is little deviation from the linear least-squares fit, resulting in an extremely small error on the estimate of the mean line-of-sight Doppler velocity. The single exception is lag 13 which is not processed for the reasons described by *Greenwald et al.* [1985].

The width of the Doppler spectrum can be inferred from the variation of the power $(R^2 + I^2)^{\frac{1}{2}}$ of the ACF as a function of lag number. We have found that the decorrelation of the ACF with time is generally best described by an exponential expression of the form

$$P(t) = C \, e^{i\omega t} \, e^{-\lambda t} \qquad\qquad [1]$$

where C is the zero lag power, ω the Doppler frequency, and λ the decorrelation parameter. The Fourier transform of P gives a Doppler spectrum of the form

$$S(\omega') = C \, \frac{2\lambda}{\lambda^2 + (\omega - \omega')^2} \qquad\qquad [2]$$

which peaks at $\omega' = \omega$ and has a full width at half maximum of 2λ rad/s.

Figure 5 illustrates the signal processing for a sample of HF radar data. Figure 5a shows the real and imaginary parts of the ACF. Figure 5b presents the Doppler spectrum that is obtained from the Fourier transformation. The phase angle variation shown in Figure 5c is best fit by a velocity of -423 m/s with an estimated error of 14 m/s. Figure 5d shows the variation of power with phase angle. Two fits to the variation are shown. That obtained from the decorrelation expression of Equation 1 is much better than the second fit, which was obtained from an expression quadratic in λ. The value of 30 Hz for λ corresponds to a half-power spectral width of 130 m/s. The vertical line on the spectrum of Figure 5b corresponds to the mean Doppler velocity computed from the fit of Figure 5c, and the horizontal bar shows the half-power width as computed from the fit of Figure 5d.
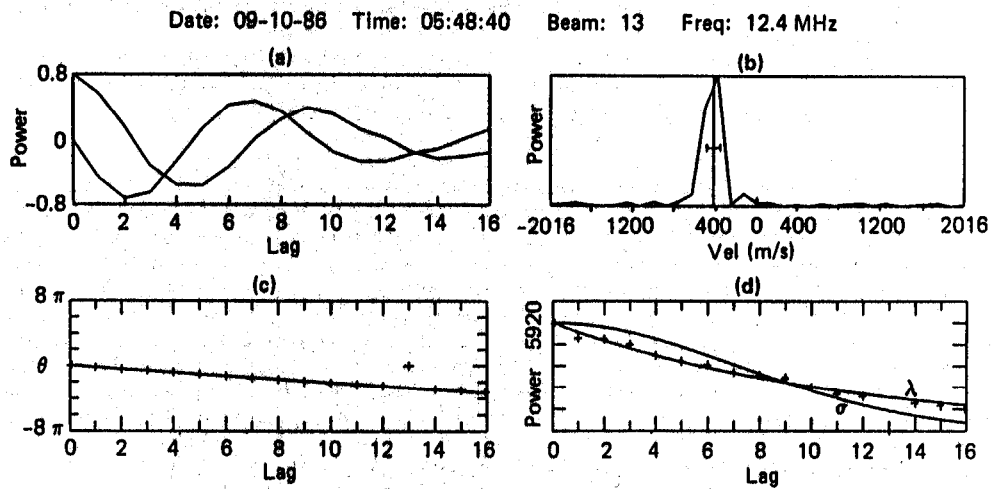
Figure 5. Stages in the processing of a sample of HF radar data. (a) Real and imaginary parts of an ACF. (b) Doppler spectrum obtained by Fourier transformation of the ACF. (c) Phase angle as a function of lag and its linear least-squares fit. (d) Power variation of the ACF as a function of lag and fits based on exponential λ and exponential $\sigma = \lambda^2$ as explained in the text. [Reprinted from Villain et al., 1987]

The Relation of Irregularity Drift To Plasma Drift

Generally, the signal backscattered to the HF radar is Doppler shifted. This corresponds to a relative line-of-sight motion of the phase fronts of the irregularity structures. Recently, studies in the high-latitude E region have demonstrated that the relationship between irregularity velocity and E X B velocity in that altitude regime is complex (i.e. *Nielsen and Schlegel* [1985]). However, studies with HF radars in the high-latitude F region indicate the direct equality of the irregularity velocity and the drift velocity of the ambient plasma [*Villain et al.*, 1985; *Ruohoniemi et al.*, 1987]. Figure 6 illustrates the results of a study carried out with the Goose Bay HF radar and the SRI incoherent scatter radar located at Sondrestrom, Greenland. Over a 40-minute period well-correlated reversals in the line-of-sight velocity of over 1 km/s were observed by the two radars.

It must be emphasized that the velocity measurement made by an HF radar in the F region is sensitive to only the plasma drift perpendicular to B, i.e. the E X B velocity. This is a consequence of the alignment of the irregularity phase fronts with the geomagnetic field lines. Thus, the motion of the irregularities in the high-latitude F region can be used to trace the ionospheric convective drift.

Localization of the HF Echo Sources

It has already been noted that ionospheric refraction is required for irregularities to be observed in the high-latitude F region. The exact path of the radar signal through the ionospheric medium is then unknown. It is important to determine how accurately the location of the echo sources can be fixed given the echo parameters at the radar, such as group delay, elevation angle, and azimuth angle. This problem has been addressed by *Villain et al.* [1984], who modelled HF ray propagation in a realistic high-latitude ionosphere derived from measurements made with an incoherent scatter radar. An example of a ray tracing is shown in Figure 7. The portions of the paths overprinted with heavy hatching indicate where the rays come to within 1° of orthogonality with B, i.e. where backscattering from small-scale irregularities is possible. Rays with low take-off angles (0-14°) reach orthogonality in the E region and are in fact entirely reflected there. Rays in the 20-30° interval penetrate the E and F regions without approaching orthogonality. In the 16-18° interval the rays penetrate the E region but come close to orthogonality in the F region. It is found that the error in the localization of the echo sources obtained by assuming a range to the scattering volume equal to the group delay range is generally less than about 50 km. This corresponds to only one range gate of uncertainty on the HF radar measurements. The sensitive calibration experiment described by *Ruohoniemi et al.* [1987] produced an empirical offset factor of just 15 km for echoes obtained from ranges of 1000 km.

IONOSPHERIC DYNAMICS

Mapping High-Latitude Plasma Convection

The HF radar technique is readily suited to studies of high-latitude plasma convection. In this section, we outline the methods developed to synthesize HF radar data into two-dimensional maps of convection velocity. A more detailed discussion can be found in *Ruohoniemi et al.* [1989].

Figure 8 shows examples of maps of velocity. Figure 8a presents line-of-sight velocity data for a 16-beam scan carried out by the Goose Bay radar. Also plotted are line-of-sight vectors for simultaneous Schefferville data. The Schefferville radar at this time (October, 1986) was operated on a single look direction. The limited region of overlap of line-of-sight
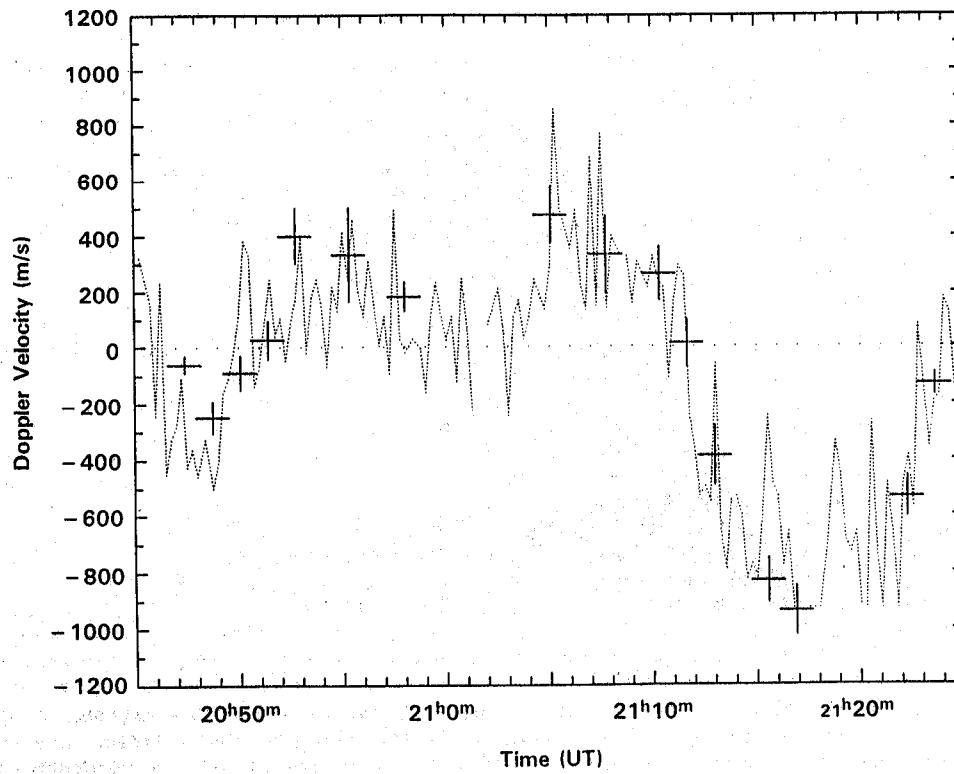
Figure 6. Comparison of time series of line-of-sight velocity estimates for a 40-minute period of coordinated Goose Bay - Sondrestrom observations. The 15-s incoherent scatter velocity data are plotted as a semi-continuous trace without error bars. [*Reprinted from Ruohoniemi et al., 1987*]
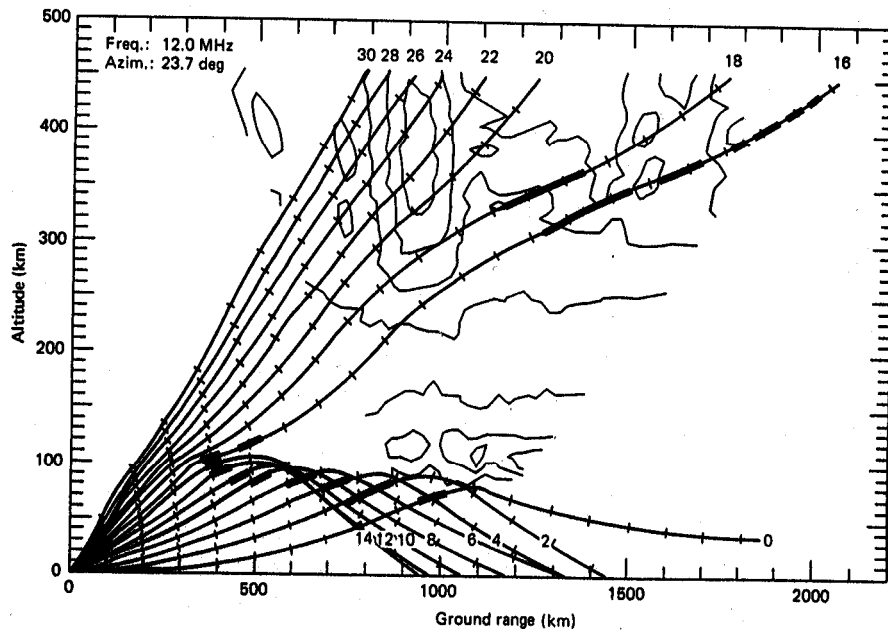
Figure 7. Ray tracing through a model ionosphere for a transmitted frequency of 12 MHz. Representative contours of the density distribution are shown. The tic marks along the traces indicate increments of 100 km in group delay. The heavy hatching shows where the rays come to within 1° of orthogonality to B. [*Reprinted from Villain et al.*, 1984]
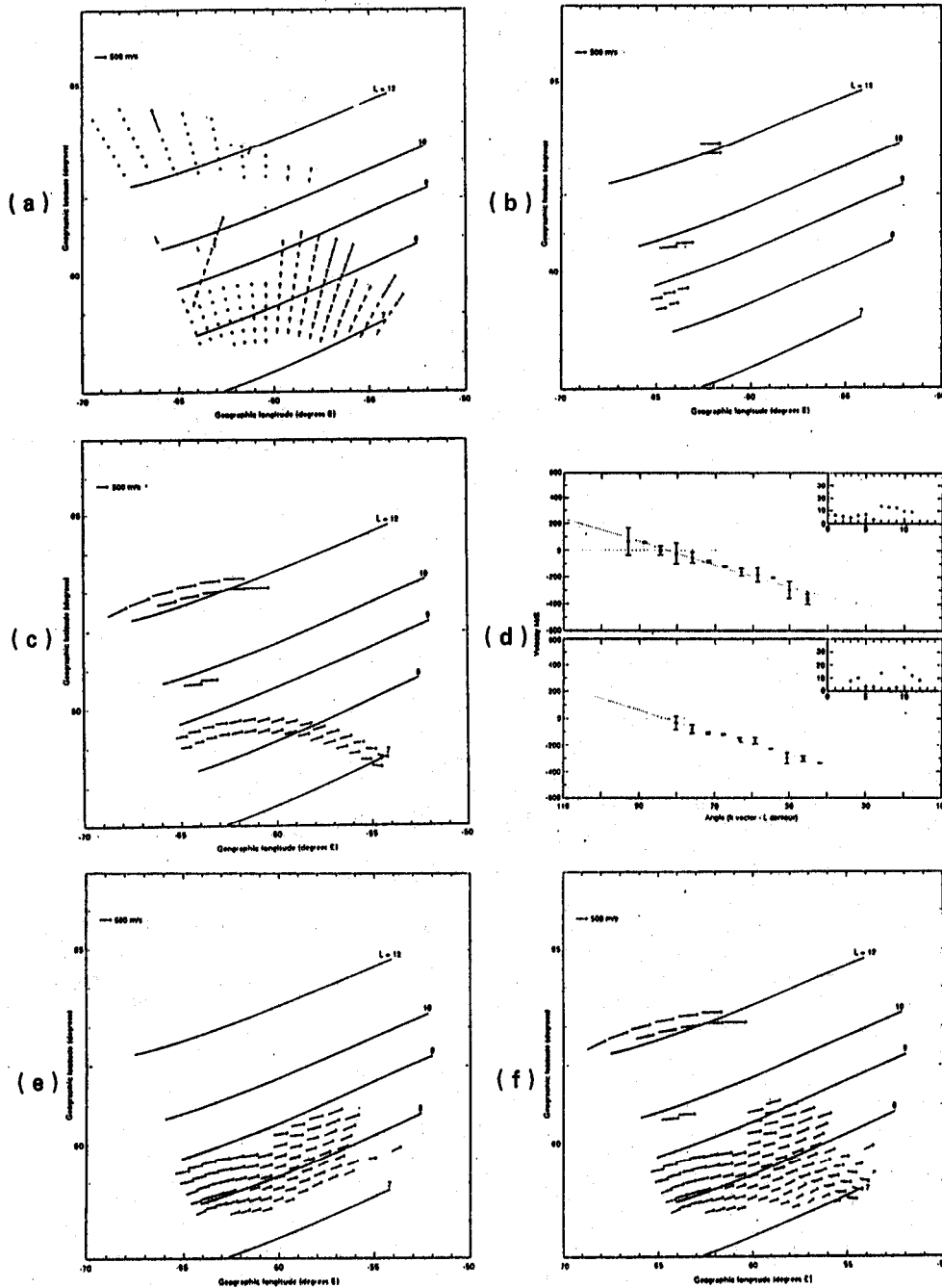
Figure 8. Sequence of plots illustrating the methods of mapping ionospheric plasma convection velocity using HF radars. For explanation, see text. [*Reprinted from Ruohoniemi et al.*, 1989]

velocity estimates can be solved vectorially for estimates of the convective drift velocity. The result is shown in Figure 8b. It is possible to extend this solution by noting that the overall velocity field must be divergence-free, i.e. $\nabla \cdot v = 0$. The result is shown in Figure 8c. Finally, the variation of the line-of-sight velocity with azimuth may indicate that the plasma drift was constant in magnitude and direction along contours of constant L shell. Figure 8d shows the result of testing this condition on the Goose Bay data of this scan; excellent least-squares fits are obtained, indicating that the drift of plasma was almost due westward along L contours and of magnitude 500 m/s. Figure 8e shows the velocity map obtained by L shell analysis of the line-of-sight velocity data from Goose Bay alone. Figure 8f superposes the vectors of Figure 8c on those of Figure 8e extended by application of the divergence-free condition. It can be seen in the regions where the vectors are double that excellent agreement is obtained between the different methods of solution.

Thus, there are several techniques for analyzing data collected with HF coherent radars for information on ionospheric convection. These consist of (i) merging line-of-sight velocity data from widely separated radars, (ii) analyzing line-of-sight velocity data for uniformity of the motion with respect to contours of constant L shell, and (iii) applying the condition that the overall flow be divergence-free ($\nabla \cdot v = 0$) to line-of-sight velocity data, with seed vector velocity data provided by method i) or ii).

Goose Bay - Sondrestrom Observations of the Polar Cleft

We illustrate the velocity mapping techniques with an example taken from a coordinated study of the polar cleft carried out with the Goose Bay radar and the SRI incoherent scatter radar located at Sondre Stromfjord, Greenland (67°N, 51°W). The incoherent scatter measurements provide estimates of the line-of-sight component of the bulk plasma motion and thus the SRI radar can serve as a second radar for vectorial analysis of the convection pattern. Figure 9a shows the overlapping maps of line-of-sight velocity estimates that were obtained during a six-minute period. It indicates that in addition to strong (> 500 m/s) flows, both radars observed dramatic reversals in the convection. The result of directly merging the two sets of velocity estimates for velocity vectors is shown in Figure 9b. (The solution is limited to pairs of vectors that intersect at angles greater than 40°.) The principal motion is a northeasterly drift. With decreasing latitude through 66° the motion turns abruptly westward. Towards the highest latitudes (> 70°) the drift rotates into a more poleward orientation.

The region of velocity vectors can be enlarged by applying the divergence-free ($\nabla \cdot v = 0$) condition to both sets of line-of-sight velocity data. The vector solutions illustrated in Figure 9b provide vector velocity estimates for initializing this analysis. Figure 9c shows the result. It is clear that the region of northeasterly flow extends to earlier local times. At the highest latitudes the flow turns poleward and westward.

In this complicated system of flows, we discern two large-scale cells of convection. The poleward cell extends from earlier local times in the cleft period and includes a substantial flow towards the polar cap. The equatorward cell intrudes into the cleft period from the afternoon sector, where the flow is predominantly westward. The combination of a shear reversal at lower latitudes with a poleward turning of the flow at higher latitudes is consistent with the post-noon Heppner-Maynard convection patterns that are obtained for the northern hemisphere under conditions of southward IMF B_z and negative B_y [*Heppner and Maynard*, 1987]. Solar wind data for this period indicate that indeed these were the orientations of the IMF components.
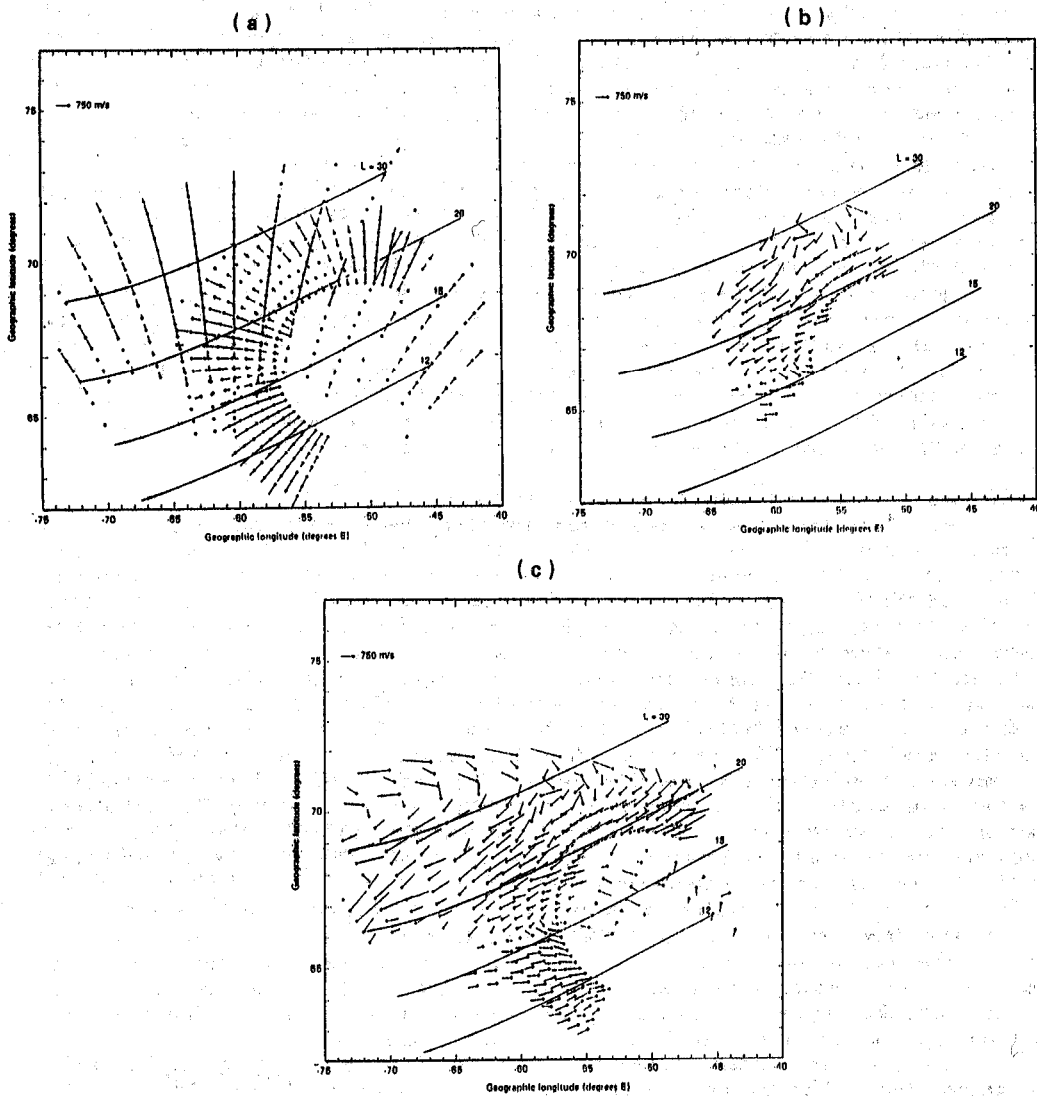
Figure 9. Sequence of plots showing the mapping of plama convection using HF coherent scatter data from Goose Bay and incoherent scatter data from the SRI radar at Sondre Stromfjord. For explanation, see text. [*Reprinted from Ruohoniemi et al.*, 1989]

IONOSPHERIC IRREGULARITIES

E Region Instability Studies: Electrostatic Ion Cyclotron Waves

The small-scale (~ 10 m) irregularities observed by coherent scatter HF radars are generated by plasma instabilities. In the high-latitude E region, the Farley-Buneman and gradient-drift instabilities are thought to account for the bulk of the observations (see *Fejer and Kelley* [1980]). However, a new type of echo has recently been identified that seems to relate to the electrostatic ion cyclotron (EIC) instability [*Villain et al.*, 1987]. We review the experimental evidence for the existence of these echoes and their origin in magnetic field-aligned electron-ion drifts.

An EIC-type event is characterized by the appearance of an L shell-aligned arc of echoes in the early morning period. The motions present within the arc tend to be slow and smoothly varying with azimuth, of such a sense as to indicate eastward motion. The most important feature is the appearance of localized regions of high Doppler velocity within the arc. The high Doppler velocities take on well-defined values in the range 350-650 m/s. Figure 10a presents a plot of the variation of the line of sight Doppler velocity with angle between k vector and L contour for a representative EIC event. The low velocity component is well-fitted by a cosine curve obtained for a drift almost due eastward along the L contour of magnitude 217 m/s. The high-velocity signal is superimposed on this smooth variation over two beams and reaches values slightly exceeding 500 m/s. The localized regions of high velocity last for periods of a few minutes to a few tens of minutes. Figure 10b shows examples of 'jumps' in line of sight Doppler velocity data plotted as a function of range for selected beams. From analysis of this sort, the existence of two types of high velocity signal can be inferred. One is distributed between 320 and 550 m/s and has an average value of 445 m/s, while the other is distributed between 500 and 650 m/s and has an average value of 580 m/s.

As discussed by *Villain et al.* [1987], the lower set of high Doppler velocities represents the ion acoustic velocity in the medium. Echoes with this phase velocity are associated with the Farley-Buneman type of instability. It is useful to plot the ratio of the two higher velocity components where their simultaneous presence could be identified from velocity jumps in the data base. This plot is shown in Figure 11. Also plotted are two curves representing the ratio of the Doppler velocities of EIC waves (V_{eic}) and the ion acoustic velocity, C_s. V_{eic} is computed from fluid theory and is controlled by three parameters: the ion cyclotron frequency Ω_i (which varies with ion mass), the irregularity wave vector k, and C_s. The ratio $R = V_{eic}/C_s$ is expressed analytically by

$$R = \frac{1}{C_s}\left[\frac{\Omega_i^2}{k^2} + C_s^2\right]^{\frac{1}{2}} \qquad [3]$$

The theoretical curves are drawn for two ion species, O^+ and NO^+. The O_2^+ curve would fall just below the NO^+ curve and the N_2^+ one just above. The excellent agreement between the experimental data and the theoretical curve for NO^+ indicates that the lower of the high-velocity modes is associated with the ion acoustic instability and the higher velocity component is associated with NO^+ EIC waves. The low velocity component (~ 200 m/s), from which the plasma drift can be inferred, appears to be related to the action of the gradient-drift instability.

It is significant that the convective plasma drift in these events is insufficient to excite the Farley-Buneman instability. *Villain et al.* [1989]
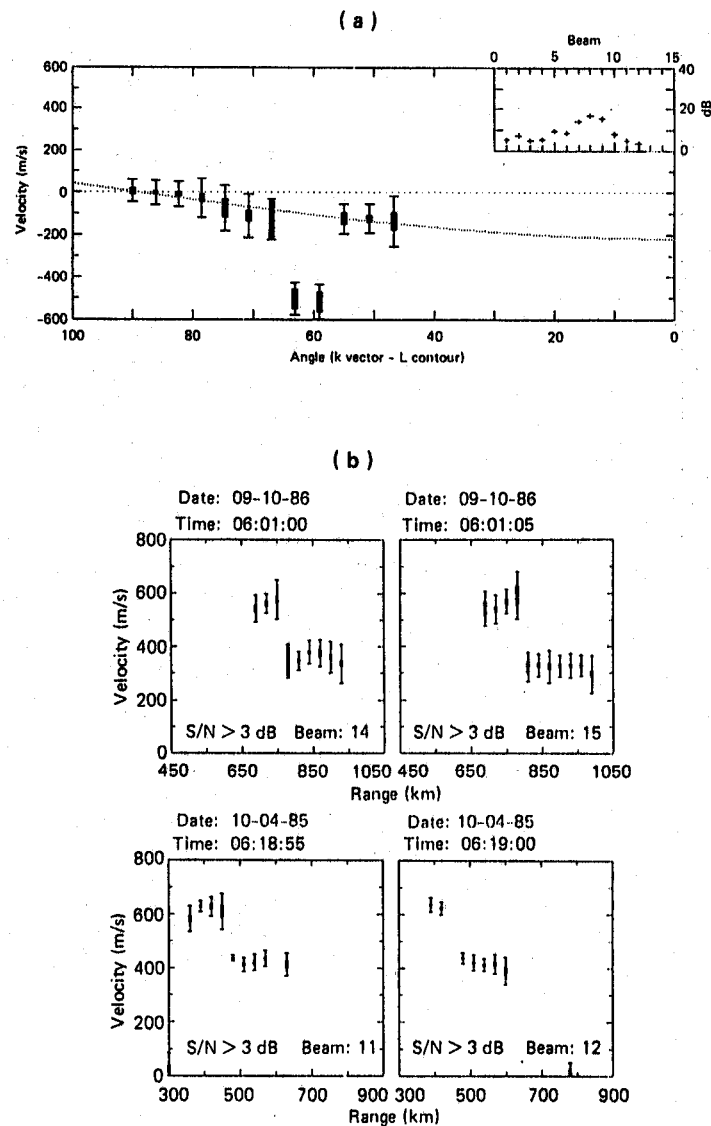
(a)

(b)

Figure 10. (a) Doppler velocity variation as a function of the angle between radar k vector and L contour for an EIC event. Note the presence of high Doppler velocity signals superposed on a background of low velocity signals. (b) Examples of transitions between high and low Doppler velocity signals. The plots show velocity as a function of range for selected beams. [*Reprinted from Villain et al.*, 1989]
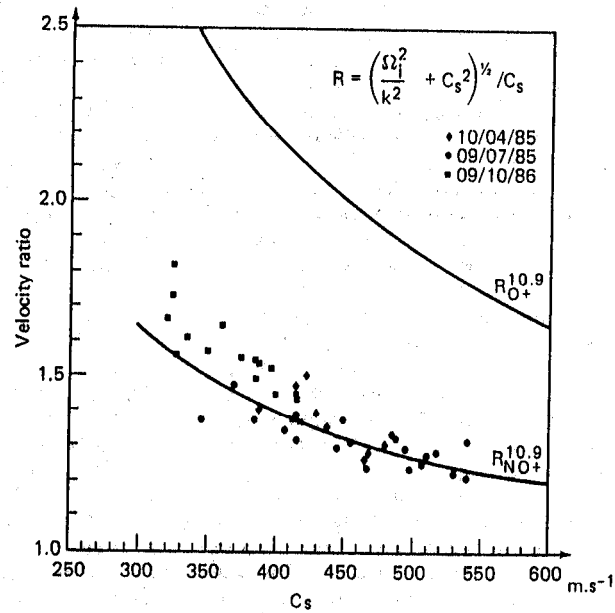
Figure 11.   Ratio between the velocities observed on either side of velocity transitions plotted as a function of the lower velocity, assumed to be C_s. The theoretical value of this ratio is plotted for O^+ and NO^+ ions. [*Reprinted from Villain et al.,* 1989]

have presented direct evidence that ion acoustic modes can be produced in regions of subcritical perpendicular drift. The clear implication is that additional destabilization of the Farley-Buneman modes occurs as a result of the field-aligned drifts. Thus, field-aligned currents may play an important role in the interpretation of 'classical' Farley-Buneman echoes as well as the more recently discovered EIC echoes.

F Region Instability Studies: The Wintertime Trough at Dusk

It has been found that there are strong diurnal and seasonal dependences in the occurrence of coherent scattering from the high-latitude ionosphere. In this section, we describe a type of activity seen with remarkable regularity in the dusk sector of the wintertime subauroral ionosphere. For a more detailed discussion of this phenomenon see *Ruohoniemi et al.* [1988].

Figure 12 shows a sequence of images obtained with the Goose Bay radar during a one-hour period of observations in the late afternoon/early evening of January 12, 1986. The feature of interest is the band of echoes just off the coast of the Quebec-Labrador land mass. It first appeared (1949:25 UT) as a few weak echoes near the eastern edge of the field of view. With time it intensified and moved westward (2011:00 UT). It was possible to track the westward movement of the most intense part of the echo activity (2021:35 UT). Eventually, the scatter weakened in the eastern sector as the activity was observed to rotate entirely out of the field of view (2037:25 UT).

This example is illustrative of a class of scatter activity called dusk scatter that is observed by the Goose Bay radar with great regularity in the wintertime ionosphere, especially during quiet geomagnetic conditions. Dusk scatter first appears when the solar zenith angle in the scattering region is near 95°. It appears to move in a westerly direction and is observed for 1 - 1½ hours. The occurrence of dusk scatter is strongly dependent on season. Figure 13a shows a histogram of the monthly probability of dusk scatter occurrence. For the winter months the rate of occurrence is virtually 100%, while for the summer months such activity is almost absent. Figure 13b shows another manifestation of the influence of season on dusk scatter occurrence. Here, the average period of occurrence for 25-day intervals is plotted as a function of day number relative to the day of winter solstice. Also plotted are contours of constant solar zenith angle ($z = 95°$, 105°) for a point lying in the latitude interval where dusk scatter is observed. It can be seen that these curves essentially constitute bounds for the occurrence of dusk scatter. Thus, there is a strong solar zenith angle factor in the time of occurrence of dusk scatter.

As elaborated in *Ruohoniemi et al.* [1988], the irregularities responsible for dusk scatter lie in the subauroral ionosphere in the range of latitudes associated with the trough. The convective plasma drifts in that region in geomagnetically quiet times tend to be low ($\lesssim$ 150 m/s) and westward in the sun-earth inertial reference frame. Density gradients associated with the trough at the afternoon solar terminator are favorable for the generation of irregularities through the gradient-drift instability. Thus, the trough at dusk is identified as a source region for small-scale irregularities.

GLOBAL MAGNETOSPHERIC DYNAMICS

Conjugate Observations of Dayside Convection

With the techniques developed to map convection with HF coherent scatter radars, it is possible to explore many questions pertaining to the nature of the magnetospheric response to the solar wind. The installation of the HF facility at Halley Station has added a dimension in global coverage [*Baker et al.*, 1989]. In this section, we briefly discuss the results of a
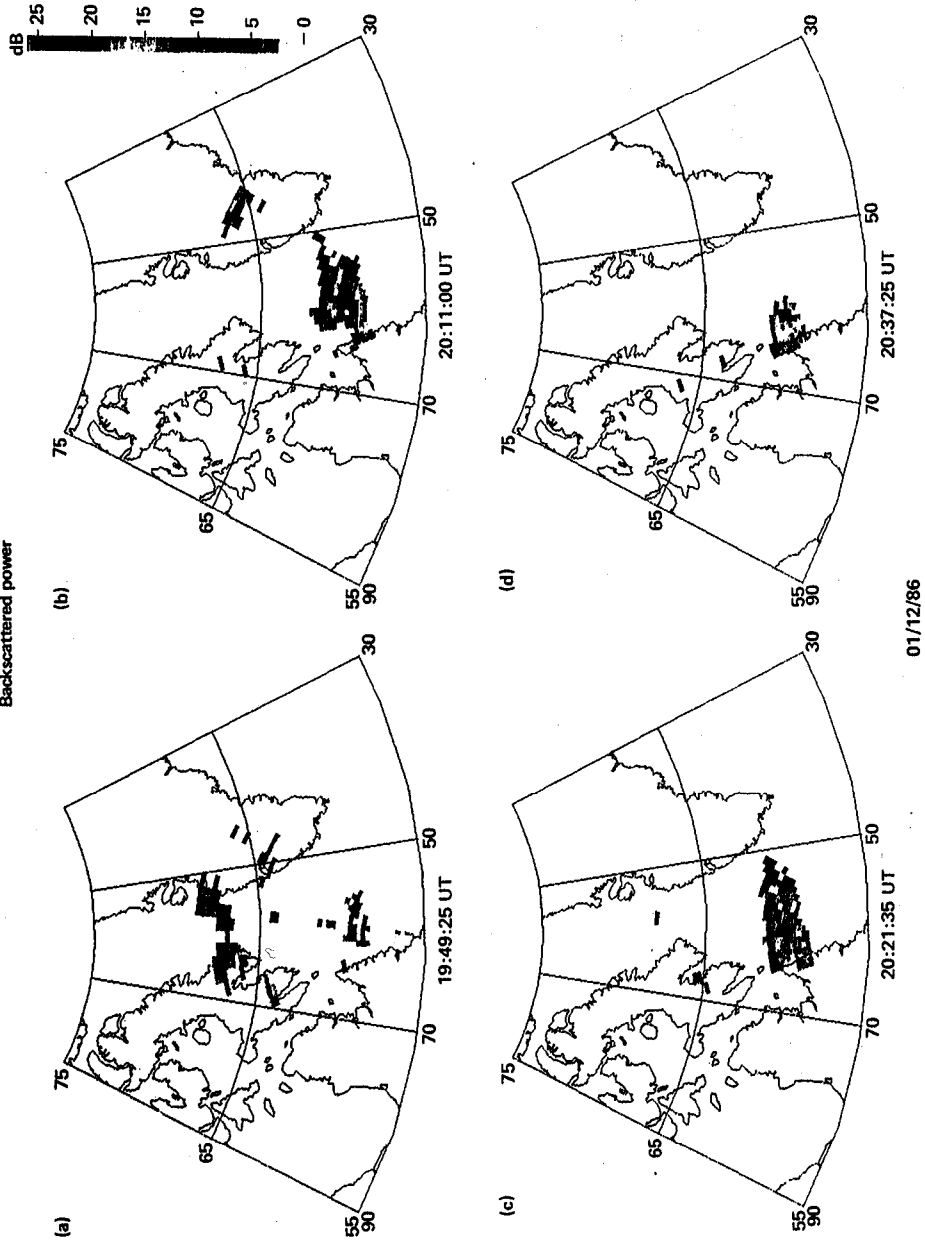
338

Figure 12. Set of four maps of backscattered power showing the development of HF backscattering activity near dusk on January 12, 1986. [*Reprinted from Ruohoniemi et al.,* 1988]
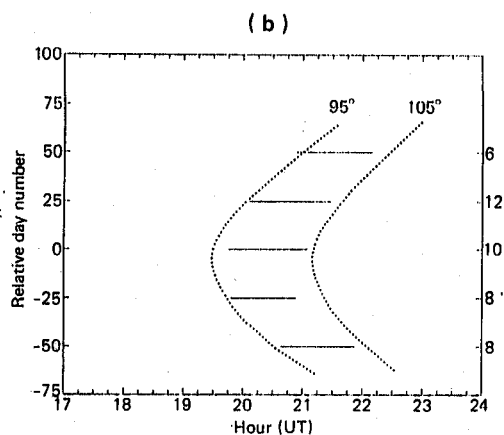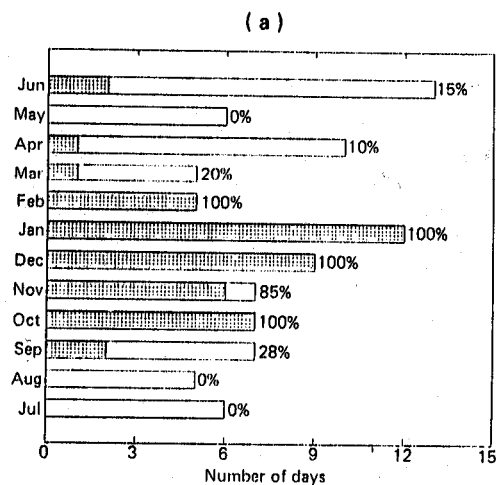
(a)

Number of days

(b)

Hour (UT)

Figure 13. (a) Monthly occurrence of dusk scattering events for magnetically quiet conditions ($K_p \leq 2$). The outer bar indicates the number of quiet days in each month. The inner shaded bar shows the number for which dusk scatter was recorded. The percentage indicates the monthly occurrence probability of dusk scatter. (b) The average period of dusk scatter for 25-day intervals centered on the day of winter solstice. The numbers along the right-hand margin indicate the number of events contributing to the calculation of each average. The dotted curves are contours of constant solar zenith angle ($z = 95°$, $105°$) for a point lying due north of Goose Bay at the range of dusk scatter. [Reprinted from Ruohoniemi et al., 1988]

coordinated Goose Bay - Halley Station study of the response of dayside convection to the IMF. A more detailed exposition may be found in *Greenwald et al.* [1989].

First, we note that the Halley Station and Goose Bay radars have a large common conjugate viewing area. Figure 14 shows this common area with the location of Goose Bay and its field of view projected onto the southern hemisphere. The conjugate mapping is performed with the aid of a magnetic coordinate system especially developed for conjugate studies by *Baker and Wing* [1989]. The conjugate area is close in size to the individual field of view of either radar ($\sim 3 \cdot 10^6$ km^2).

The observations described here were obtained during a geomagnetically disturbed period in which the radars were located in the noon local time sector. Magnetic field measurements were made in the solar wind by the IMP-8 satellite; plots of the IMF data are presented in Figure 15. During the period of interest (1445-1600 UT) B_y underwent a number of reversals while B_z remained negative. It is interesting to consider the convection patterns predicted by the Heppner-Maynard model for these conditions (*see Heppner and Maynard* [1987]). These are shown in Figure 16 for the northern hemisphere. Note that the convection patterns predicted for the southern hemisphere are complementary in the sense that the northern pattern for $B_y<0$ applies to the southern hemisphere for $B_y>0$ and vice versa. The dominant feature of the the northern hemisphere $+B_y$ pattern is the strong westward flow across local noon into a throatlike region in the prenoon sector. The principle characteristic of the $-B_y$ pattern is the clockwise rotation of the flow in the post noon sector with increasing latitude.

We now turn to maps of the convection velocity obtained with the HF radars. These are shown in Figure 17. In Figure 17*a* the Goose Bay data show uniform poleward and westward flow across the entire local noon time sector. The Halley Station map shows a sharp clockwise turning of the flow with latitude. The IMF data indicate that the B_y component was positive during this time interval (1530-1540 UT). The match with the Heppner-Maynard patterns for this orientation of B_y is very close. Figure 17*b* shows the convection maps obtained for an interval in which B_y was negative (1453-1511 UT). It is clear that the convection patterns are exchanged between the hemispheres on change of sign of the B_y component, as predicted by the Heppner-Maynard model.

We conclude that in this event the instantaneous convection patterns observed in conjugate hemispheres were consistent with the statistical patterns of *Heppner and Maynard* [1987]. In addition, we can utilize the fine temporal resolution ($\sim 1\frac{1}{2}$ min) of the HF radar observations to study the details of the transition between convection states. As discussed in *Greenwald et al.* [1989] it is found that the average time between an IMF transition at the IMP-8 satellite and the beginning of a convection reconfiguration in the ionosphere was 8 minutes. The newly reconfigured convection pattern typically filled the radar field of view (10°-15° of invariant latitude and 2$\frac{1}{2}$ hours of local time) within 6 minutes of reconfiguration onset.

The studies with Halley Station are continuing and promise to touch on very basic questions regarding the global dynamics of the magnetosphere and hemispheric conjugacy.

IONOSPHERE-THERMOSPHERE COUPLING

Goose Bay Observations of Atmospheric Gravity waves

The previous examples involved measurements of the drift of small-scale irregularities within the convecting ionosphere. We now turn to a study in which the motion of ionospheric layers themselves is directly measured by the
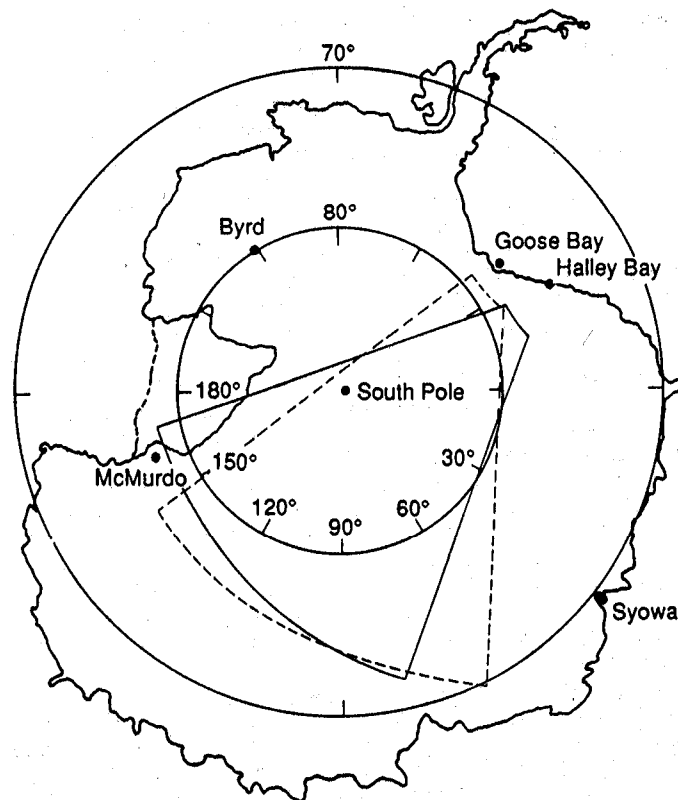
Figure 14.   Plan view of Antarctica showing the field of view of the Halley Station radar (*solid trace*).   Also shown is the conjugate location of the Goose Bay radar and the conjugate mapping of its field of view (*dashed trace*). [*Reprinted from Greenwald et al.*, 1989]

IMP - 8 Magnetometer
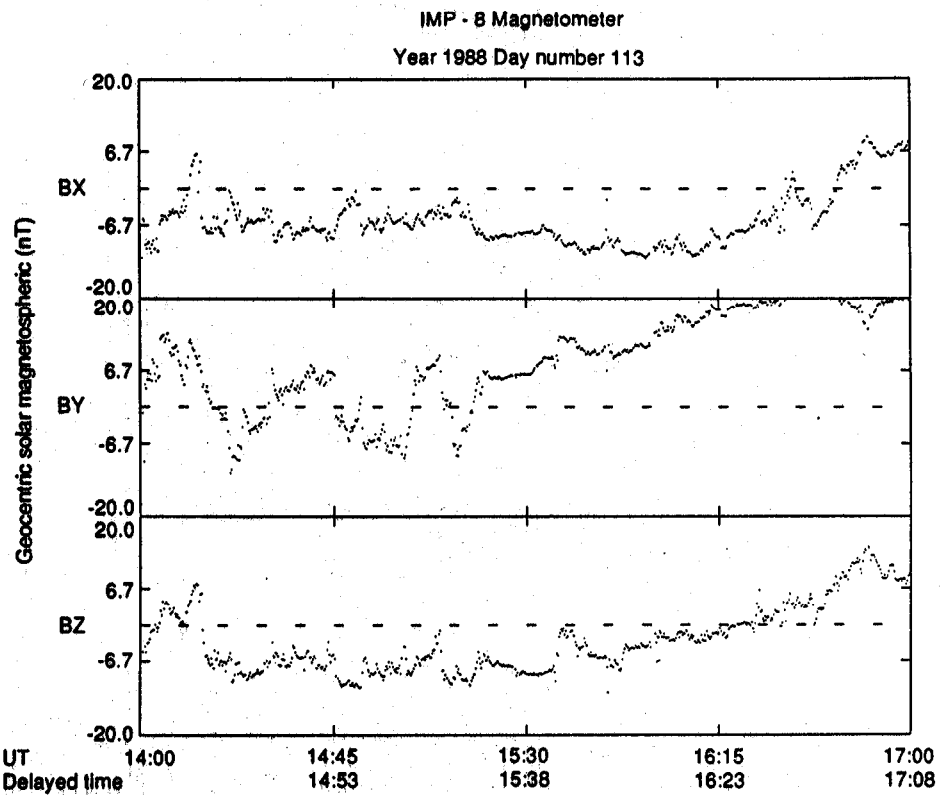**Year 1988 Day number 113**

Figure 15.   Magnetometer data from the IMP-8 satellite for April 22, 1988, 1400-1700 UT.   A second "delayed time" axis is obtained by adding 8 minutes to the UT time.   This delay is the empirically determined response time between an IMF B_y state change at the satellite and the onset of a convection response in the ionosphere. [Reprinted from Greenwald et al., 1989]

Heppner-Maynard "BC" pattern
Northern hemisphere
(a)
By<0   Bz<0

Heppner-Maynard "DE" pattern
Northern hemisphere
(b)
By<0   Bz<0

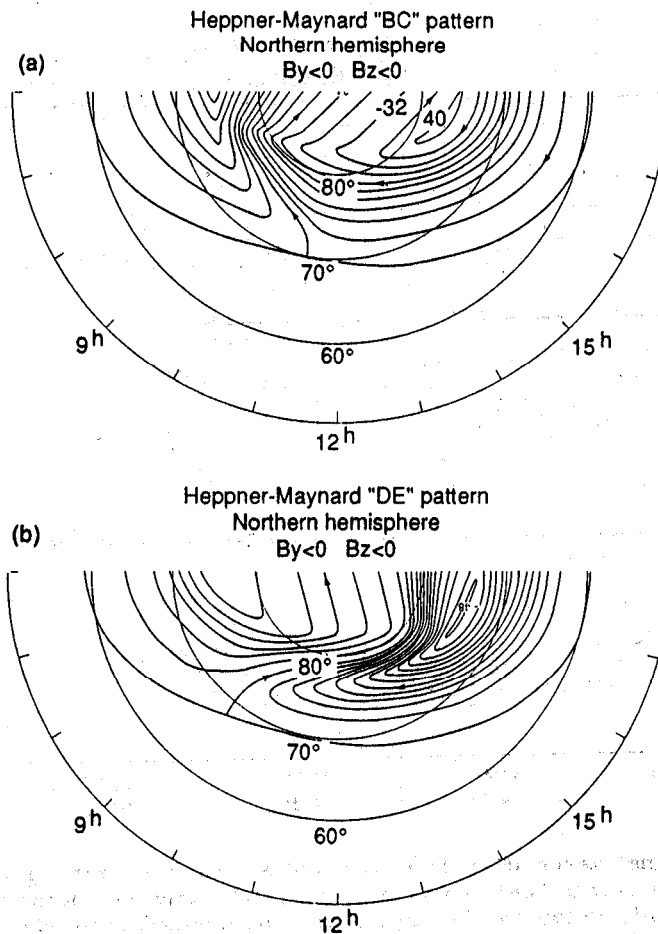Figure 16.   Dayside high-latitude ionospheric convection patterns derived by *Heppner and Maynard* [1987] for IMF $B_z < 0$ conditions: (a) BC pattern for northern hemisphere with IMF $B_y > 0$ or southern hemisphere with IMF $B_y < 0$. (b) DE pattern for northern hemisphere with IMF $B_y < 0$ or southern hemisphere with IMF $B_y > 0$. [*Reprinted from Greenwald et al.,* 1989]

(a)

Goose bay HF radar
1988/4/22

(b)

Goose bay HF radar
1988/4/22

Halley bay HF radar
1988/4/22
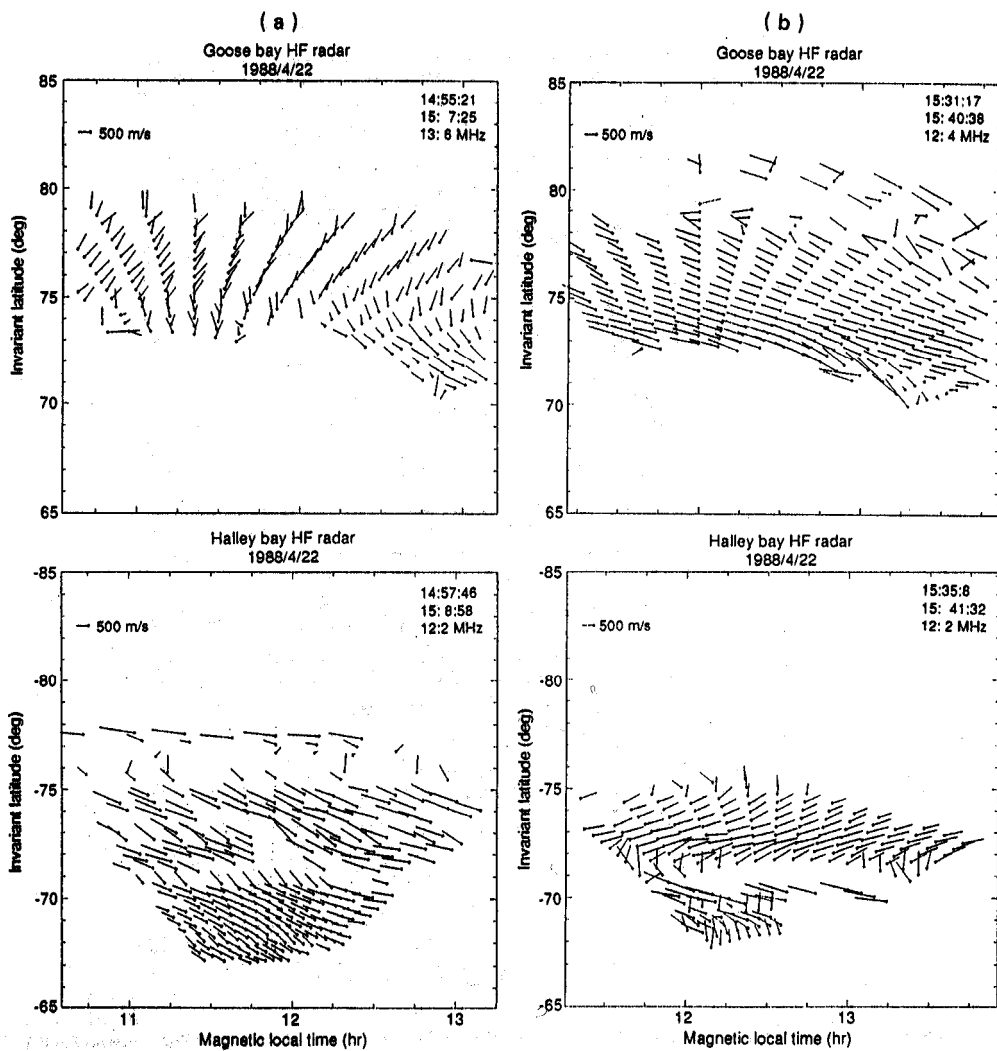
Halley bay HF radar
1988/4/22

Figure 17.   Simultaneous convection patterns in the dayside ionosphere as observed with the Goose Bay and Halley Station radars. (a) Period for which $B_y > 0$. (b) Period for which $B_y < 0$. [*Reprinted from Greenwald et al.*, 1989]
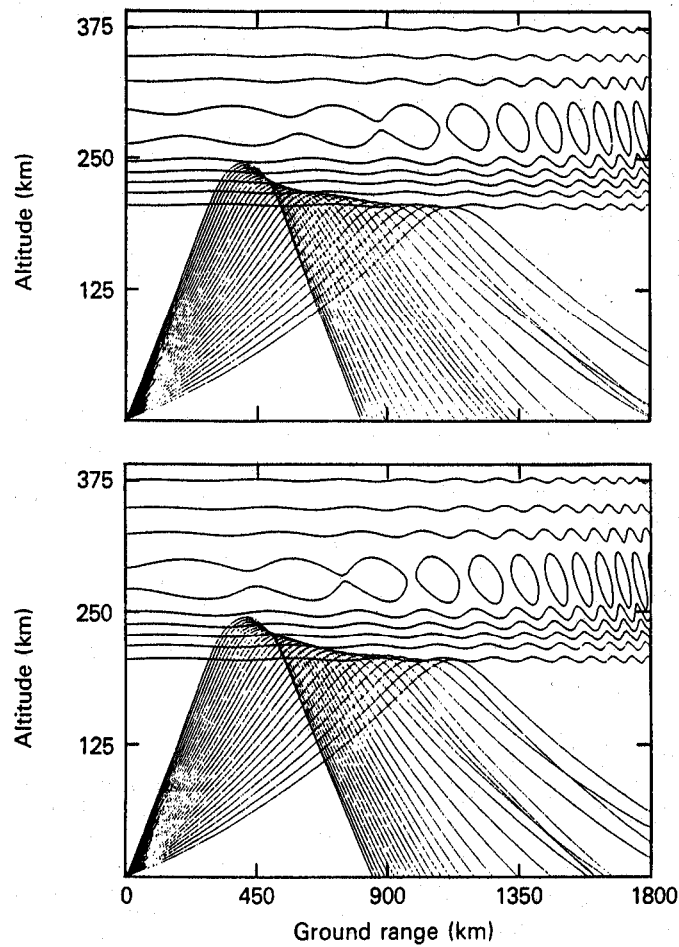
Figure 18.   Ray paths of HF signal through an ionosphere modulated by an earth-reflected gravity wave.   Note the focusing caused by the surfaces of the density minima.   Top: 195 minutes after excitation; Bottom: 210 minutes after excitation. [*Reprinted from Samson et al.*, 1989b]

Goose Bay radar. Furthermore, we will show that the motion of the layers is due to the passage of gravity waves in the neutral atmosphere and derive important parameters describing the propagation of the gravity waves. This work has been described in detail by Samson et al. [1989a] and Samson et al. [1989b].

Gravity waves propagating in the neutral ionosphere induce electron density perturbations that can be likened to corrugation-type fluctuations in the ionospheric layers. Figure 18 illustrates the propagation of HF radar signals in an ionosphere disturbed by the passage of a gravity wave. The ray paths in Figure 18a show three regions where the rays are focused. The first is the usual focus near the mimimum 'skip' distance, while the second and third are due to focusing of the rays that are reflected by the corrugation minima in the perturbed electron densities. When the radar waves are backscattered by the ground, the focused rays show up as enhanced intensities at the corresponding ranges. Note that the regions of localized intensification are related to specific phase surfaces of the gravity wave. Figure 18b illustrates the ray path focusing after a delay of 15 minutes. The focusing from the more equatorward electron density minimum is no longer obvious since it has merged with the skip distance focusing. The more poleward region is focused at a nearer range and a new region of focusing is forming at a more distant range.

Figure 19a shows the theoretical prediction for the movement of constant phase surfaces of the gravity wave from a high latitude source region toward the Goose Bay radar. This range-time plot applies to observations on one beam of the Goose Bay radar. From this theoretical phase map, it is possible to determine the time and range at which the gravity wave was generated by extending the measured phase surfaces to the position where they intersect on the range-time plane. The same procedure can be followed with experimental data. Once the direction of propagation, range, and time have been estimated, the altitude of the source can be determined by comparing the data with phase surfaces computed for sources at different altitudes.

We now consider a sample of Goose Bay data that has been subjected to the analysis outlined above. Figure 19b shows a filtered range-time plot of backscattered intensity obtained from observations made with the Goose Bay radar on November 25, 1988. Also plotted are the theoretical surfaces of constant phase for a gravity wave event scaled to have the time of onset (1211 UT) at the range (2100 km) indicated by the radar data and an altitude of 125 km. The fit is excellent. Figure 19c shows that the time and location of the onset coincided with the development of a strong velocity shear in the vicinity of the high-latitude convection reversal boundary. Thus, it would appear that a strong equatorward-propagating gravity wave was initiated by a shear reversal intensification in the high-latitude electrojet.

Many parameters describing the propagation of gravity waves can be derived. For example, it has been found that the waves propagate very nearly equatorward across contours of constant L shell from high-latitude source regions. Occasionally, waves can be seen propagating poleward from the convection reversal region. The frequencies associated with the waves cover the range 0.3-0.6 mHz; the wavelengths, 300-500 km, and the average phase velocities, 110-180 m/s. The waves propagate in a mode that penetrates through the lower atmosphere and then reflects from the earth's surface. The vertical motions of the layers that accompany passage of the gravity waves can be measured from the slight motions imparted to the signal by the movement of the reflecting layers. One interesting point is that the gravity waves tend to be seen by the Goose Bay radar in the late fall and early winter. The reason may be that conditions for localized enhancements of the high-latitude electrojet are more favorable when particle precipitation can act on an ionosphere in relative darkness.
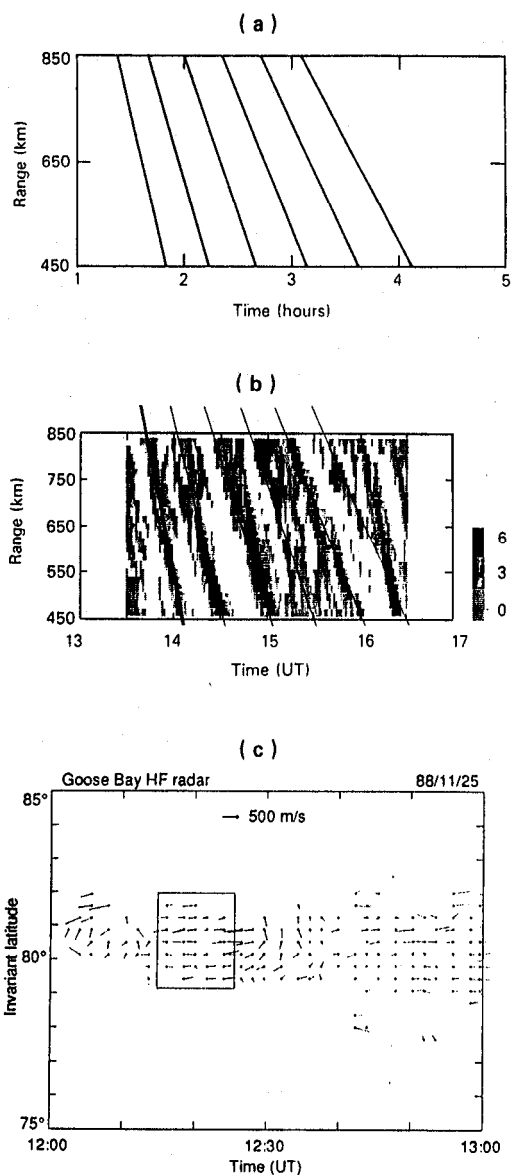
(a)

(b)

(c)

Figure 19. (a) Theoretical phase map for an earth-reflected gravity wave with a source at a range of 2000 km and an altitude of 130 km. The observation altitude is assumed to be 250 km. (b) A comparison of the best-fit theoretical phase map with the power recorded on a Goose Bay radar beam during a gravity wave event. (c) Time-series plot of the latitudinal profile of ionospheric convection for the period preceding the Goose Bay gravity wave event. The formation of the indicated velocity shear coincides with the onset of the gravity wave at very high latitudes. [Reprinted from Samson et al., 1989b]

It is clear from the foregoing that HF coherent scatter radars are a powerful tool for the investigation of high-latitude gravity wave phenomena.

CLOSING COMMENT

The HF coherent scatter technique is broadly applicable to the goals of the WITS program, especially as concerns the study of ionospheric-magnetospheric dynamics, ionospheric plasma instabilities, and ionosphere-thermosphere coupling. The scope for this work has been considerably increased through the addition of an HF radar facility in Antarctica. The operation of these HF radars is extremely flexible and adaptable to the interests of researchers in the community. This flexibility extends to real-time control of the radar and monitoring of the backscattering activity during campaign periods. The results presented in this brief survey represent only a sampling of the scientific potential of the instruments. Many other topics remain for investigation. The authors welcome the involvement of WITS researchers in the planning, execution, and analysis of future HF radar experiments.

ACKNOWLEDGEMENTS

REFERENCES

Baker, K. B., R. A. Greenwald, J. P. Villain, and S. Wing, Spectral characteristics of high frequency (HF) backscatter for high latitude ionospheric irregularities: preliminary analysis of statistical properties, *Scientific report to the Rome Air Development Center*, RADC-TR-87-284, 1988.

Baker, K. B., R. A. Greenwald, J. M. Ruohoniemi, J. R. Dudeney, M. J. Pinnock, N. Mattin, and J. M. Leonard, PACE: Polar Anglo-American conjugate experiment, in press, EOS, 1989.

Baker, K. B., and S. Wing, A new magnetic system for conjugate studies at high latitudes, *J. Geophys. Res.*, 94, 9139, 1989.

Bates, H. F., and P. R. Albee, Aspect sensitivity of F-layer HF backscatter echoes, *J. Geophys. Res.*, 75, 165, 1970.

Fejer, B. J. and M. C. Kelley, Ionospheric irregularities, *Rev. Geophys. Space Phys.*, 18, 401, 1980.

Greenwald, R. A., K. B. Baker, R. A. Hutchins, and C. Hanuise, An HF phased-array radar for studying small-scale structure in the high-latitude ionosphere, *Radio Sci.*, 20, 63, 1985.

Greenwald, R. A., K. B. Baker, J. M. Ruohoniemi, J. R. Dudeney, M. Pinnock, N. Mattin, J. M. Leonard, and R. P. Lepping, Simultaneous conjugate observations of dynamic variations in high-latitude dayside convection due to changes in IMF B_y, submitted, *J. Geophys. Res.*, 1989.

Heppner, J. P. and N. C. Maynard, Empirical high-latitude electric field models, *J. Geophys. Res.*, 92, 4467, 1987.

Keskinen, M. J., and S. L. Ossakow, Theories of high-latitude ionospheric irregularities: A review, *Radio Sci*, 18, 1077, 1983.

Nielsen, E., and K. Schlegel, Coherent radar doppler measurements and their relationship to the ionospheric electron drift velocity, *J. Geophys. Res.*, 90, 3498, 1985.

Ruohoniemi, J. M., R. A. Greenwald, K. B. Baker, J. P. Villain, and M.A. McCready, Drift motions of small-scale irregularities in the high latitude F region: an experimental comparison with plasma drift motions, *J. Geophys. Res.*, 92, 4553, 1987.

Ruohoniemi, J. M., R. A. Greenwald, J.-P. Villain, K. B. Baker, P. T. Newell, and C.-I. Meng, Coherent HF radar backscatter from small-scale irregularities in the dusk sector of the sub-auroral ionosphere, *J. Geophys. Res.*, 93, 12871, 1988.

Ruohoniemi, J. M., R. A. Greenwald, K. B. Baker, J.-P. Villain, C. Hanuise, and J. Kelly, Mapping high-latitude plasma convection with coherent HF radars, in press, *J. Geophys. Res.*, 1989.

Samson, J. C., R. A. Greenwald, J. M. Ruohoniemi, and K. B. Baker, HF radar observations of atmospheric gravity waves in the high-latitude ionosphere, in press, *Geophys. Res. Lett*, 1989a.

Samson, J. C., R. A. Greenwald, J. M. Ruohoniemi, A. Frey, and K. B. Baker, Goose Bay radar observations of earth-reflected atmospheric gravity waves in the high-latitude ionosphere, submitted, *J. Geophys. Res.*, 1989b.

Villain, J. P., R. A. Greenwald, and J. F. Vickrey, HF ray tracing at high latitudes using measured meridional electron density distributions, *Radio Sci.*, 19, 359, 1984.

Villain, J. P., G. Caudal, and C. Hanuise, A SAFARI-EISCAT comparison between the velocity of F region small-scale irregularities and the ion drift, *J. Geophys. Res.*, 90, 8433, 1985.

Villain, J. P., R. A. Greenwald, K. B. Baker, and J. M. Ruohoniemi, HF radar observations of E region plasma irregularities produces by oblique plasma streaming, *J. Geophys. Res.*, 92, 12327, 1987.

Villain, J. P., C. Hanuise, R. A. Greenwald, K. B. Baker, and J. M. Ruohoniemi, Obliquely propagating ion acoustic waves in the auroral E-region: further evidence of irregularity production by field-aligned electron streaming, submitted, *J. Geophys. Res.*, 1989.